

DUAL THERMOGRAPHIC MONITORING OF Ti-6AL-4V CYLINDERS DURING DIRECT LASER DEPOSITION

G. Marshall¹, W. J. Young II¹, N. Shamsaei^{1,2}, J. Craig³, T. Wakeman³, S. M. Thompson^{1,2,†}

¹ Department of Mechanical Engineering, Mississippi State University, Mississippi State, MS 39762 USA

² Center for Advanced Vehicular Systems, Mississippi State University, Starkville, MS 39759 USA

³ Stratronics, Inc., Lake Forest, CA 92630 USA

† Corresponding author:

REVIEWED

Email: thompson@me.msstate.edu

Phone: (662) 325 1535

Abstract

Understanding the thermal phenomena associated with Direct Laser Deposition (DLD) is necessary to begin manipulating fabricated part properties. In this study, a thermally monitored Laser Engineered Net Shaping (LENS) system is used with time-invariant (uncontrolled) build parameters to construct Ti-6Al-4V cylinders with two different build paths. Both paths utilize a circular contour with serpentine hatch fill; however, successive layer patterns are varied and the effects compared between 90° and 120° angular pattern shifts. During fabrication, the part's thermal history and melt pool temperature are recorded via an in-chamber infrared (IR) camera and a dual-wavelength (DW) pyrometer, respectively. These tools are used for non-destructive thermographic inspection (NTI) of the part to ensure target quality and/or microstructure. A unique calibration method for the IR camera utilizing the DW pyrometer data is presented and a calibration correction factor was utilized for high temperature ranges. The melt pool was found to be 40-50% superheated reaching temperatures up to 2500 °C at times. Temperature characteristics of two different layers were compared for different hatching patterns, and the results show that for a given point in time, maximum temperatures can vary based on laser raster. Temperature gradients varied and peaked at about 1000 °C/mm along the diameter of the small rods. This can lead to anisotropy in microstructural and mechanical properties allowing for unique property growth per build path. Cooling rates within the melt pool appear to increase as maximum melt pool temperature increases, for instance, from 16,000 °C/s – 41,000 °C/s.

Introduction

Laser Engineered Net Shaping (LENSTM) is a Direct Laser Deposition (DLD) process first developed by Sandia National Laboratories [1]–[4]. This laser-based additive manufacturing (LBAM) technology has the potential to reduce production costs by lowering the amount of time and material required for fabrication. Direct Laser Deposition utilizes a slice file created from a 3-D Computer Aided Design (CAD) solid model to deposit a geometry one layer at a time. Each layer is deposited in tracks by feeding metal powder into a laser-formed melt pool onto a substrate. Before the benefits of DLD can be fully realized, a firm knowledge base must be developed to characterize the effects of DLD process parameters - such as laser power, travel speed, and powder feed rate - on a part's thermal history, which in turn determines its final microstructure and mechanical properties.

The length and maximum temperature of the melt pool increases with laser power and slower travel speeds. As the melt pool moves, its tail rapidly solidifies and experiences the highest cooling rates [5] and these rates increase with travel velocity [6]. During DLD, delivered laser energy is transferred by conduction away from the melt pool through previous layers and the substrate while the remainder contributes towards melting and vaporization or is transferred away from the surface by convection and radiation [7]. Maximum DLD Ti-6Al-4V melt pool temperatures can be up to 40% above their liquid temperature (i.e. superheat). Furthermore, local melt pool temperature gradients and peak cooling rates for parts undergoing DLD have been experimentally and numerically assessed at 100 °C/mm – 1000 °C/mm [3], [8]–[11] and 12,000 °C/s – 25,000 °C/s [12], [13] .

For the *uncontrolled* DLD process, in which time-invariant process parameters are employed, the final part microstructure is greatly prone to anisotropy. This is due to many thermal-fluidic phenomena, including: localized heating from the laser, non-uniform thermal gradients, solidification and time-dependent cooling rates. Better understanding of the sensitivity of such thermal phenomena to the uncontrolled DLD process parameters can allow for their easier manipulation for minimizing anisotropy. One way of controlling heat transfer, and thus final product quality, in both LENS and other DLD or cladding processes, is to use nondestructive thermographic inspection (NTI) for generating data to be used in feedback control [4], [14]–[16]. For example, one can relay melt pool temperatures to a laser controller for microstructural uniformity throughout a part by compensating laser delivery based on local heat transfer [16]. Common tools used for LBAM monitoring include infrared (IR) cameras and dual-wavelength (DW) pyrometers [2], [3], [17]–[19].

In order to effectively utilize an IR camera for monitoring absolute temperature of a part during DLD (or laser cladding), the spectral/directional, temperature-dependent surface emissivity must be known. Due to radiation noise in a typical DLD chamber, and the transient nature of surface emission, determining the surface emissivity can be very challenging if not impossible. Thus, in-lieu of determining the absolute temperature distribution of a part, one can opt to utilize relative temperature gradients provided by IR images. However, Griffith et al. suggested that, if a valid expression for effective wavelength (as a function of temperature) is known, then one can employ Wein's Law to determine absolute temperature [8].

There has been some recent work focused on calibrating IR cameras for use in LBAM processes. In 2005, Yang et al. showed that the emissivity of Ti-6Al-4V remained relatively constant (at ~0.25) between 132 °C to 800 °C after which point it varied up to 0.98 at 1029 °C due to severe oxidization [20]. Doubenskaia et al. experimentally determined the emissivity of Ti-6Al-4V during a Nd:YAG laser cladding process purged with argon [21]. By using a MICRON M390 to find brightness temperature with the IR camera, an emissivity of 0.201 was determined in the phase transition temperature of the metal. Actual temperature was then found by using the brightness temperature at liquid-solid transition, the determined emissivity, and the grey body assumption [21]. Rodriguez et al. determined the emissivity of Ti-6Al-4V during a Selective Laser Melting (SLM) process to be 0.26 between 650 °C and 750 °C (similar to [20] and [21]) and 0.5 in powder form [22]. These values along with reflected temperature and optics transmission were used to calculate actual surface temperature which was validated by using

thermocouples during the build. Actual temperatures varied from the recorded IR temperatures by a near-constant value.

Pyrometers are an attractive means for non-contact temperature measurements in DLD processes as they are able to measure high temperatures ($>1000\text{ }^{\circ}\text{C}$) [16]–[19], [23], [24]. They are, therefore, ideal for measuring melt pool temperatures that can exceed the liquidus temperature of, say, Ti-6Al-4V – at $1636\text{ }^{\circ}\text{C}$. A DW pyrometer may be selected to reduce the error caused by sensitivity to emissivity [13]. Utilization of two wavelengths allows for more accurate surface temperature measurements by using the ratio of the relative radiation intensity at both wavelengths [12], [13]. Many have used thermal monitoring for characterizing maximum temperatures and cooling rates of a bulk part and melt pool during DLD, and relating them to the microstructure and mechanical properties of parts [2]–[4], [8], [15], [17], [19], [25]. For instance, Kobryn et al. mapped out solidification rates using thermography while experimenting with various lasers in an additive cladding process. Solidification rates were then used to justify the microstructure seen in the final parts [25]. Nassar et al. related thermal history to the growth of microstructure and hardness along the height-wise direction of a build [16].

This current work focuses on utilizing LENS for fabricating Ti-6Al-4V cylindrical specimens while monitoring their bulk and melt pool temperature responses, via in-chamber IR camera and DW pyrometer, respectively. A demonstration of dual thermography of cylindrical specimens during LENS and a unique approach for calibrating the high-end temperature of an IR camera using online pyrometer data is provided. Thermographic images of the melt pool and bulk part are provided. The effect of scan strategy (i.e. build pattern) on the temperature and melt pool response is discussed, in addition to typical heating and cooling rates and temperature gradients in vicinity of the heat affected zone (HAZ).

Experimental Setup and Procedure

Experiments were conducted to observe build pattern effects on part/pool thermal signatures at various layers, as well as to determine a correction factor (CF) for the IR camera for DLD of Ti-6Al-4V. An Optomec LENSTM 750 DLD system (chamber shown in Figure 1) with a 1 kW Nd:YAG laser was used for part fabrication. Titanium alloy (Ti-6Al-4V) powder (Phelly Materials Inc.), manufactured via a Plasma Rotating Electrode Process (PREP) with -100/+325 mesh size was used. The powder was deposited onto a $152.4 \times 152.4 \times 3.175\text{ mm}^3$ Ti-6Al-4V substrate placed atop a 6.4 mm thick copper spacer-plate that was attached to a moving build stage.

The following parameters were utilized (values approximate): 350 W laser power, 16.9 mm/s scan speed, and 0.13 g/s powder feed rate. The DLD chamber was sealed and purged with argon during all builds. Cylindrical specimens, $\text{Ø} = 6.6\text{ mm}$ and 78.2 mm tall, were fabricated using a 5.08 mm layer thickness and hatch spacing (each specimen was a total of 154 layers). Two different build strategies, characterized by unique hatching (contour fill) patterns (Pattern A and B) were examined in this study. For both patterns, the outer circumference of the rod was deposited first in a counter-clockwise direction, followed by alternating tracks to fill in the circle as shown in Figure 2. Pattern A designates a 0° , 90° , 180° , and 270° repeating sequence of the aforementioned track deposits while Pattern B designates a 0° , 120° , and 240° repeating

sequence. It is of interest to note that Ensz et al. demonstrated that a build strategy consisting of 105° track rotations between layers can be optimal for fabrication of cylindrical parts via LENS [26]. However, this current study is more concerned with the thermal response measurement, and not the optimization, of hatch patterns.

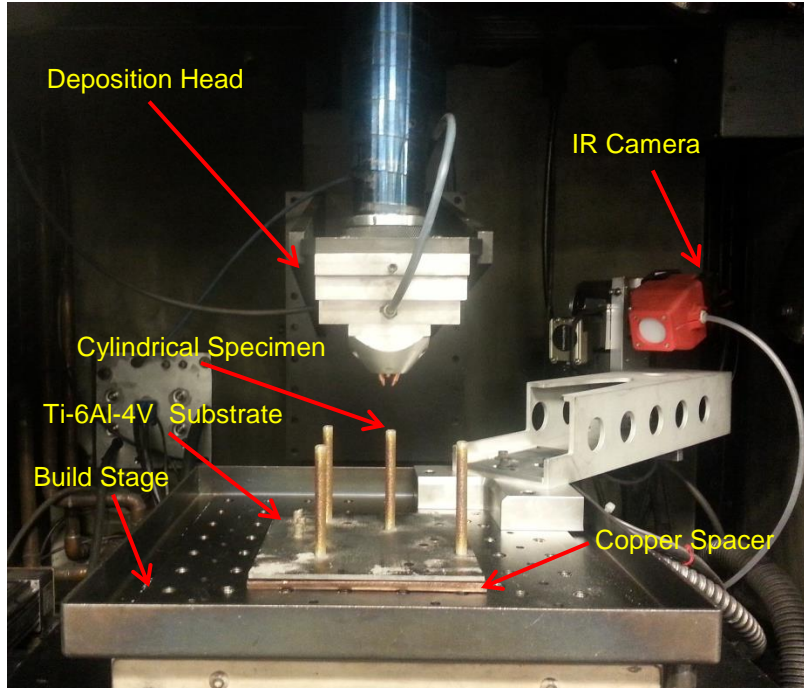


Figure 1. Photograph of Optomec LENS 750 chamber with deposition head, substrate, spacer and custom-installed IR camera.

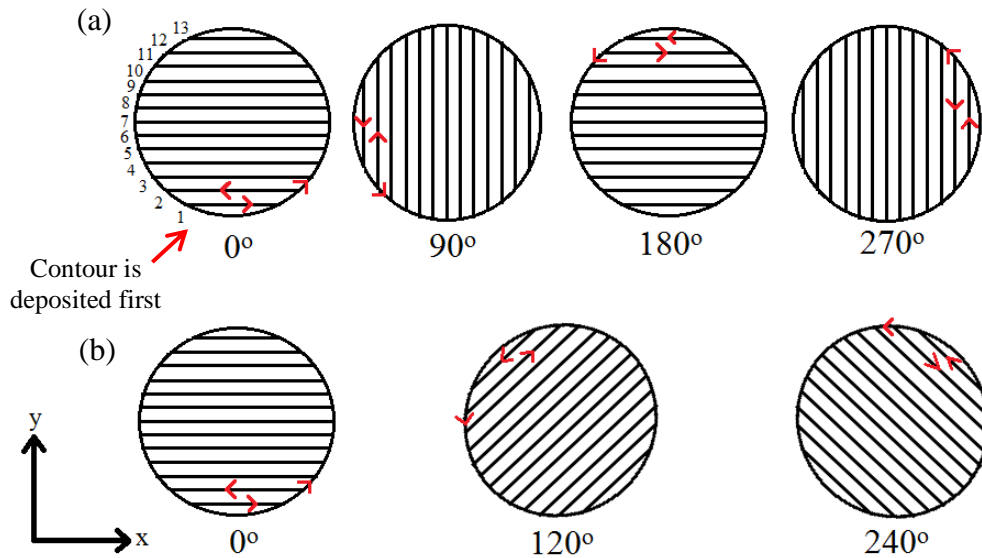


Figure 2. Contour deposit and hatch raster pattern and order for LENS: (a) Pattern A: 90° rotations for each layer and (b) Pattern B: 120° rotations for each layer.

As shown in Figure 1, an IR camera (Stratronics) was attached to the build stage within the LENS chamber to allow for monitoring of the exposed part surface and HAZ during the build. Using this setup, the *deposition head* appeared to be moving during visualization as the tracks were deposited. The IR camera was positioned approximately 101.6 mm above the substrate and pointed 10° (from vertical) towards the build, as shown in Figure 3, which also shows the focal plane and a few layer numbers. During experiments, the IR camera was set to capture images at 14 Hz. In addition to the IR camera, a DW pyrometer (Stratronics), located atop and outside the LENS chamber, was utilized for monitoring melt pool temperature (and indirectly, melt pool geometry and size). As shown in Figure 3, the DW pyrometer was mounted in such a way that its line-of-sight was directed down the deposition head column to the melt pool. The DW pyrometer possessed a 16 micron/pixel resolution and a 4 mm field of view. Using *Stratronics ThermaViz* software, the DW pyrometer was set to capture images while in the ‘free-run’ setting, resulting in an acquisition frequency between 4 - 7 Hz. For calibration and comparison, melt pool and bulk temperature data were extracted from a ‘measurement line’ along the left edge (relative to camera point of view) of the rod as shown in Figure 3.

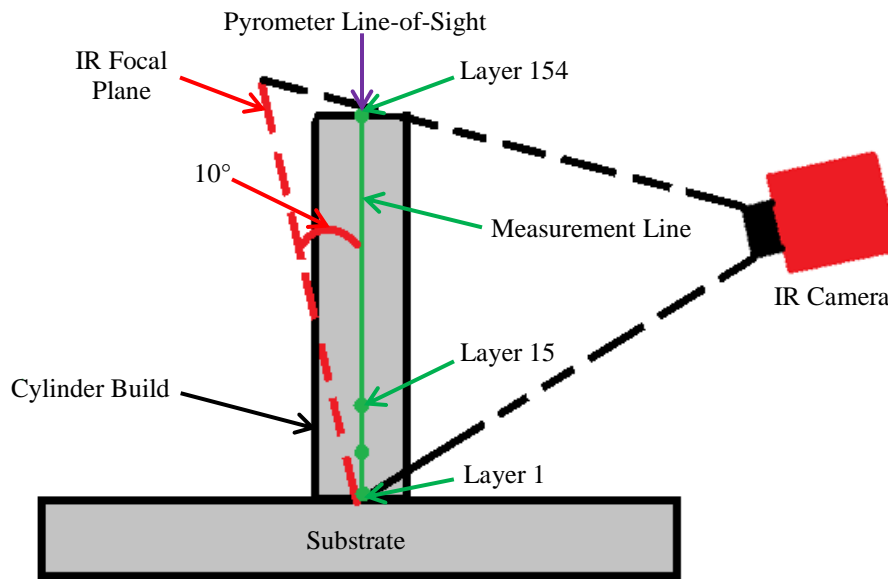


Figure 3. Side view of the IR camera focal plane which is oriented ~10° from vertical, including: arbitrarily-selected layer numbers, DW pyrometer line-of-sight, fictitious measurement line, completely-built cylinder and the substrate.

Infrared Camera Calibration

The as-received DW pyrometer was calibrated using a high-temperature tungsten filament at known temperature. Since DW pyrometers provide for relatively accurate temperature measurements at each point along a layer during metallic deposition [20], the in-phase DW pyrometer and IR data, collected along the measurement line, were utilized for high-temperature calibration of the IR camera. The in-phase, maximum IR measurements and average melt pool temperatures at the measurement line were employed; corresponding to the deposition of the circular contour for each seventh layer. The melt pool temperature was quantified using the mean of all values greater than the liquidus temperature of Ti-6Al-4V (1636

°C [27]) along fictitious lines parallel and perpendicular to the melt pool's maximum temperature zone. Absolute maximum temperature of the melt pool was also recorded. As shown in Figure 3, the cylindrical rods were placed on the center of the substrate to ensure their relative position to the IR camera focal plane was known with reasonable accuracy. Note that, for the current setup, the IR temperature error increases with layer number due to the focal plane diverging from the measurement line.

Figure 4 provides the in-phase maximum, raw IR measurements and separate melt pool temperatures (from the DW pyrometer) as recorded upon intersection of the melt pool (during the initial layer contour deposit) with the measurement line while employing either Pattern A or B. For the calibration, the corresponding, maximum melt pool IR signature was assumed equivalent to the average temperature of the melt pool from the pyrometer.

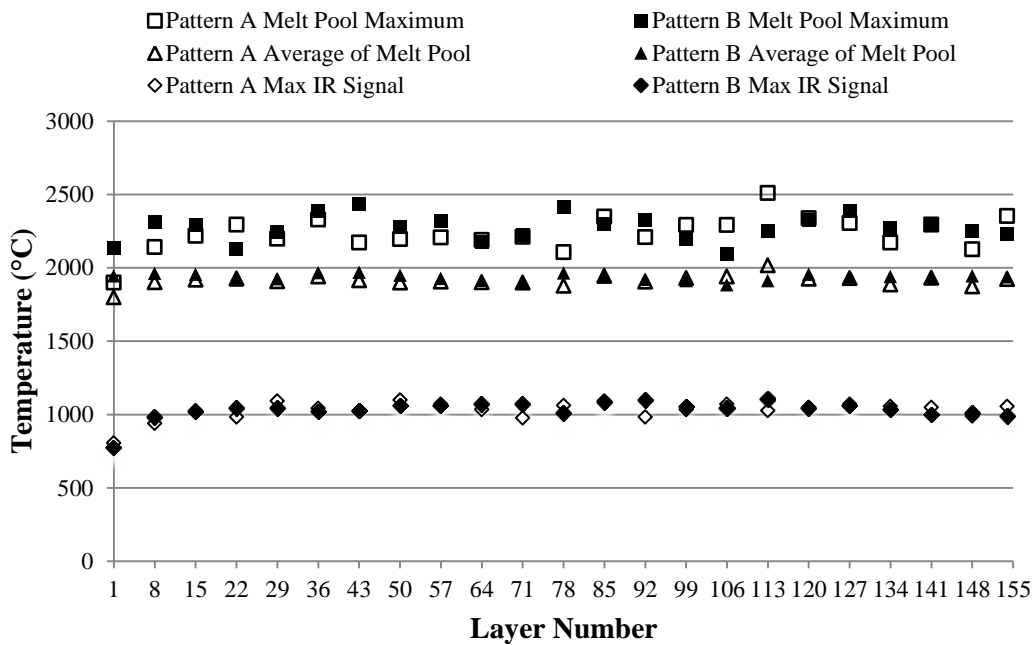


Figure 4. Comparison between in-phase IR signal of melt pool at measurement line and either maximum or average melt pool temperature (measured via pyrometer) as measured during Pattern A and B deposits.

From Figure 4, it is clear that both build patterns have similar average melt pool temperatures and IR values throughout the build; however, the melt pool's maximum temperature seems to vary more since the starting point of the contour deposit can vary between both build patterns. If a measurement was taken at the beginning or end of a deposited contour where the melt pool velocity approaches zero, the melt pool would be expected to have a higher temperature [6]. The maximum melt pool temperature is found to vary between ~ 2,100 °C and 2,500 °C during contour deposition and be almost independent of deposition pattern. The average melt pool temperature was found to vary between 1,900 °C and 2,000 °C during contour deposition. These pyrometer measurements indicate that the Ti-6Al-4V melt pool can be 20 - 50% superheated above its liquidus temperature. Note that both the melt pool temperature and IR signal were lower during the deposition of initial layers.

Each raw, uncorrected *IR data point* was corrected to absolute temperature via summation of a correction factor [22], and this method is herein utilized by use of pyrometer data shown in Figure 4. A correction factor (CF) of $CF \approx 886$ was found by taking the average difference between each raw IR data point and its corresponding pyrometer temperature measurement for Pattern A. Since the emissivity of molten Ti-6Al-4V varies only slightly in an inert environment [20], [22], the *CF* was assumed constant regardless of temperature. This appears to be an accurate assumption, since, as shown by Figure 5, the difference between the maximum IR signal and average melt pool temperature is approximately constant for both deposition patterns. The percent relative error between pyrometer/melt-pool temperature and post-calibrated IR temperature is provided in Fig. 5. It can be seen that the average, relative error is approximately 2%, with maximum error occurring during deposition of Layer 1, corresponding to 5.9% for Pattern A and 14.6% for Pattern B.

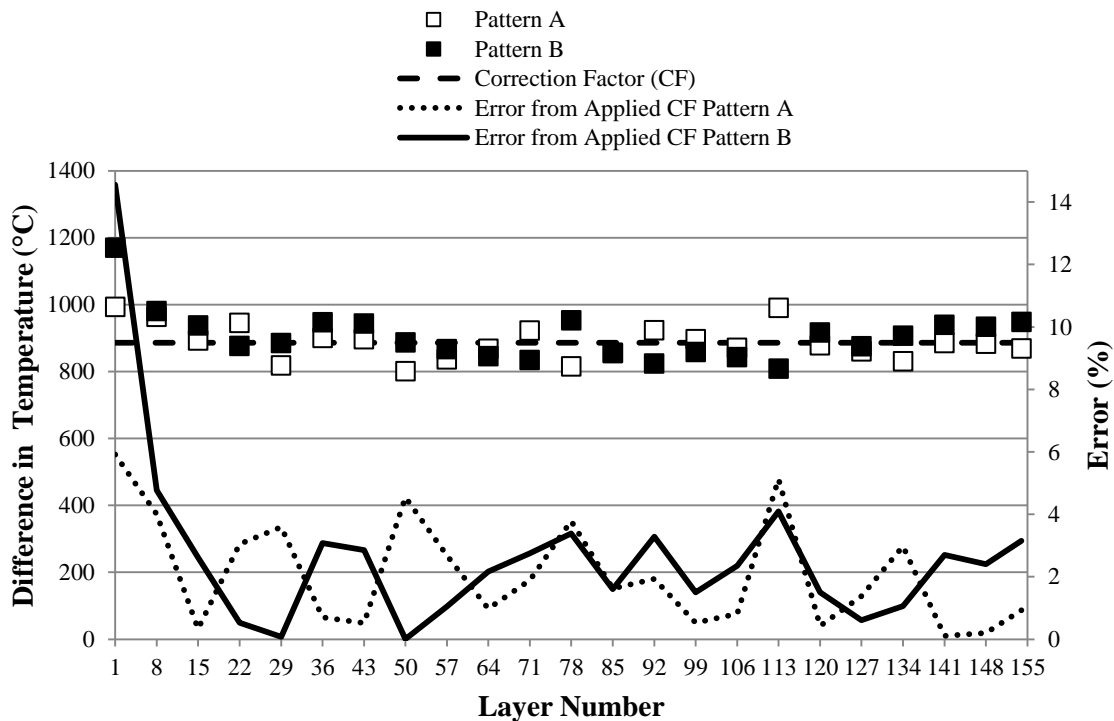


Figure 5. Difference in measurement and percent relative error between calibrated, maximum IR temperature and average melt pool temperature for Pattern A and B.

Results & Discussion

The melt pool and part temperature response during contour deposition for Layer 85 and Layer 148 are shown in Figure 6 and Figure 7, respectively. Note that the white lines in Figure 6 and Figure 7 represent the line along which a measurement was taken. All pyrometer images (melt pool) are shown on a scale from 1400 °C – 2400 °C while the IR images are shown on the same scale only for the enclosed calibrated regions.

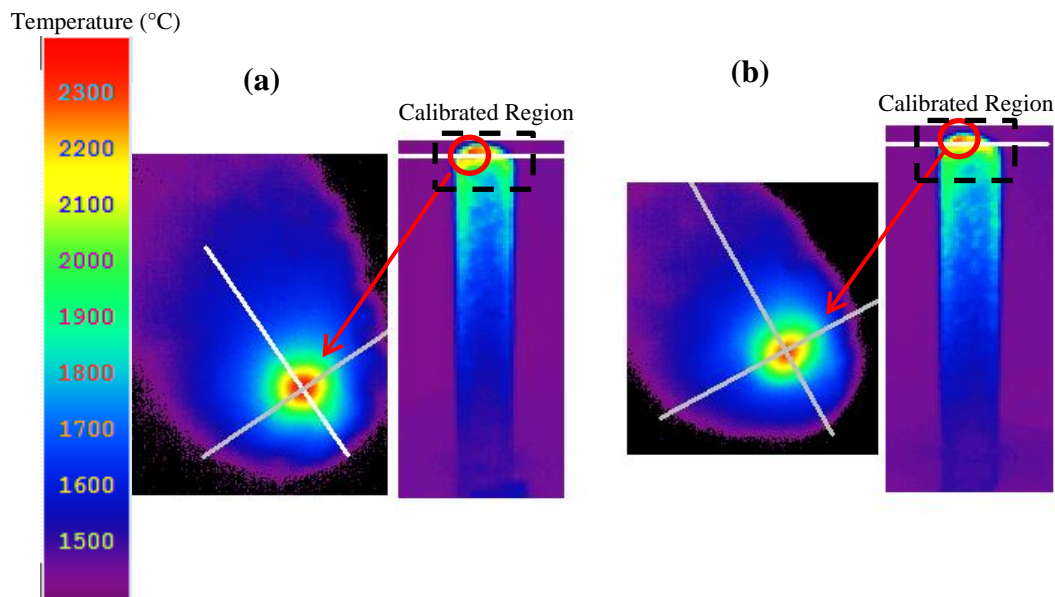


Figure 6. Thermographic images (melt pool captured by pyrometer on left and IR temperature distribution on right) collected simultaneously during contour deposit of Layer 85 for (a) Pattern A and (b) Pattern B. For the bulk temperature distribution, the scale is valid for the dashed box region only.

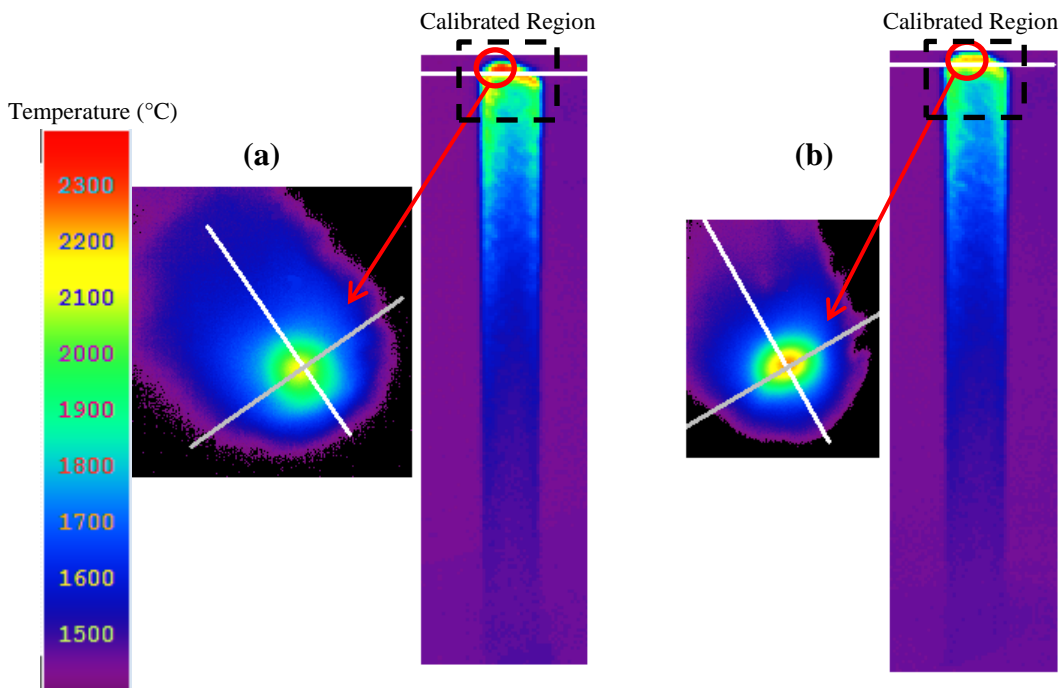


Figure 7. Thermographic images (melt pool captured by pyrometer on left and IR temperature distribution on right) collected simultaneously during contour deposit of Layer 148 for (a) Pattern A and (b) Pattern B. For the bulk temperature distribution, the scale is valid for the dashed box region only.

For Pattern A, the maximum melt pool temperature was slightly higher than for Pattern B in Layer 85 – a difference of about 52 °C, but the average temperature for both was about 1940 °C. The general shape of the melt pool temperature contour is also similar for both patterns

shown in Figure 6. Both build patterns were laying their tracks at 0° rotation and were thus identical; therefore, one would expect such similar results from the thermal data. A 121 °C and 73 °C temperature difference exists between the maximum melt pool and average melt pool temperatures respectively at Layer 148 as shown in Figure 7 – with Pattern B being the greater. The diameter of the melt pool is also smaller here in Pattern B and suggests that the laser has just begun its contour movement; whereas, Pattern A seems to have been half-way through its deposit. Since the laser’s velocity at the beginning of the contour is zero, this creates a build-up of heat and a more concentrated melt pool. The melt pool begins to cool and lengthen as the velocity is increased as Figure 7 (a) suggests. At this point in time, Pattern B is laying a 0° rotation track while Pattern A is laying a 270° rotation track; therefore, one could expect a variation in temperature measurements as evidenced in the data. Though these maximum and average temperatures are well above any phase transformation range, their difference in magnitude still agrees that variations in microstructural and mechanical properties can exist within a part under certain conditions due to temperature.

Cooling rates were found by taking the spatial derivative along the direction of melt pool travel, i.e. subtracting neighboring temperatures and dividing by the distance between them. The following equation may be applied to find cooling rates within the melt pool [13]:

$$C_r(t) = \frac{\Delta T_{mp}}{\Delta x_{avg}} s$$

where $C_r(t)$ is the cooling rate as a function of layer; ΔT_{mp} is the change in temperature between averaged points in the melt pool that are an average distance of Δx_{avg} apart; and s is the laser scan rate equal to 16.9 mm/s. The locations of greatest slope, i.e. maximum cooling rate, were found at the tailing end of the melt pool as a preliminary step. Figure 8 gives an example of such location. Next, three temperature points taken from the DW pyrometer data for a single melt pool image were averaged on both sides of the location of maximum temperature change within the melt pool and then subtracted from one another to give a ΔT_{mp} . An optical calibration determined the distance between pixels to be about 0.014 mm making $\Delta x_{avg} = 0.042$ mm when the locations corresponding to the temperatures on either side of the maximum change location were averaged and subtracted.

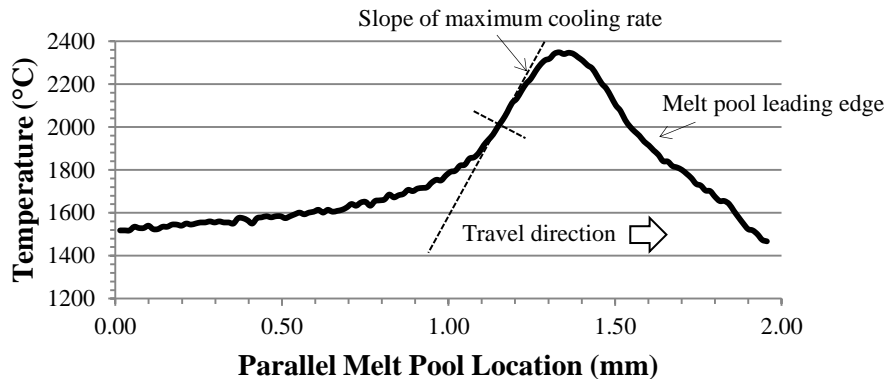


Figure 8. Maximum cooling rate (slope) for Layer 85 of Pattern A. Data averaged on either side of location of maximum slope.

Values for the cooling rates are shown in Table 1 as well as the pattern rotation deposited at the current layer number. The data shows that the first layer has the lowest cooling rate. Profiles of the melt pool at this first stage are still developing; therefore, the calculated slopes were less in this layer than the other observed layers. Both patterns experience an increase in cooling rate in the middle layers. At these points, the melt pool has had time to develop – creating larger cooling rates within the melt pool temperature profile. Pattern B’s cooling rate is still greater in Layer 148 compared to Layer 85 – its maximum temperature is increasing (see Figure 4), and the temperature slopes become steeper. However, a comparison between Pattern A’s Layer 148 and Layer 85 shows a decrease in maximum temperature. Along with the temperature decrease, the pattern is also different. As previously mentioned, the data suggested that Pattern B was near the beginning of its contour deposition which created elevated temperature over Pattern A. With similar average melt pool temperatures, an increase in maximum melt pool temperatures corresponds with an increase in cooling rate. Others have seen cooling rates of 25,000 °C/s [13] and 12,000 °C/s [12]. These cooling rates are comparable to tabulated in Table 1; however, the increased scan speed as compared to [13] has caused these results to exceed 25,000 °C/s.

These melt pool cooling rates should not be confused with bulk cooling or solidification rates that will exist in a fabricated part. For instance, bulk cooling could be expected to be greater in the first few layers as the substrate acts as a heat sink.

Table 1. Estimated cooling rates associated with three different layers for each pattern.

Layer Number	Pattern A		Pattern B	
	Cooling Rate (°C/s)	Pattern Rotation (°)	Cooling Rate (°C/s)	Pattern Rotation (°)
1	15,661	0	16,060	0
85	41,675	0	33,844	0
148	24,156	270	41,144	0

The temperature gradient along six layers measured by the IR camera is shown in Figure 9. These measurements were taken when the melt pool was located relative to the measurement line in the IR image of Figure 3. Temperature distributions per layer were very similar between the two patterns – the maximum signal reached throughout the build was close to 1986 °C. Since temperature is shown as estimated actual temperature, only data with an IR signal above 800 °C (the minimum range of this study) has been considered and calibrated. Location along the diameter of the rod was found by first noting the pixel at which IR signal began to increase. Then, the last point at which the temperature decreased was considered to be at the outer diameter of the part (6.6 mm). Distance between pixels was then found to be about 0.367 mm. Discrepancies between each patterns’ contours of Layers 113 and 154 respectively may be attributed to the IR camera being slightly out-of-focus for these layers.

Spatial temperature distribution data from the IR camera can be derived by subtracting neighboring temperature values and dividing by the distance between pixels – about 0.367 mm – to create the plots shown in Figure 10. These plots show the small distances over which large amounts of power are absorbed that can lead to anisotropic mechanical and microstructural

properties. One trend seems to be that this radial gradient decreases with an increase in layer number.

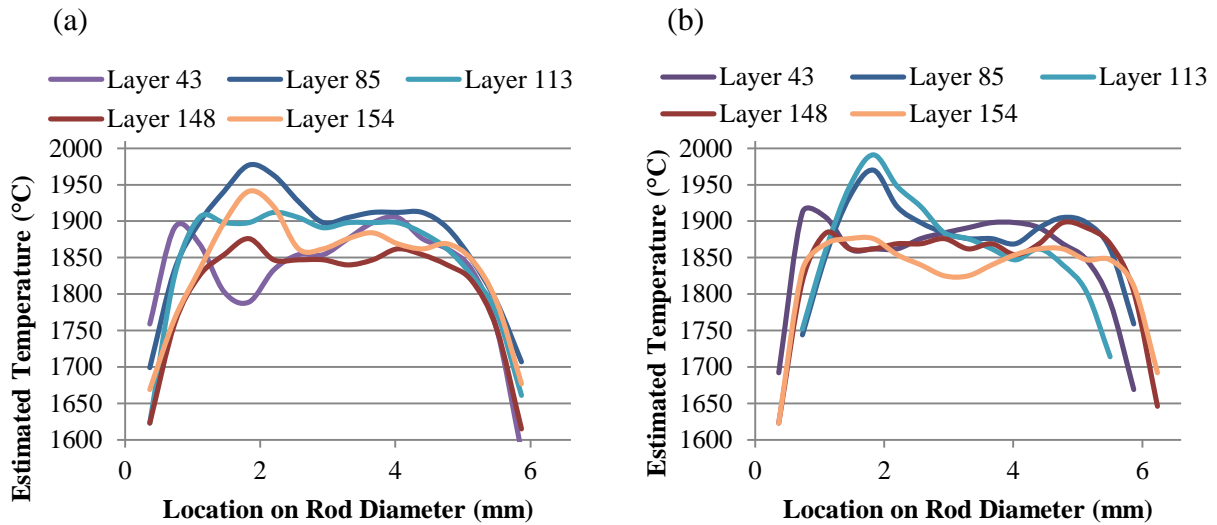


Figure 9. Temperature profile measured by the IR camera along the diameter of the rod at the melt pool for different layers of (a) Pattern A and (b) Pattern B.

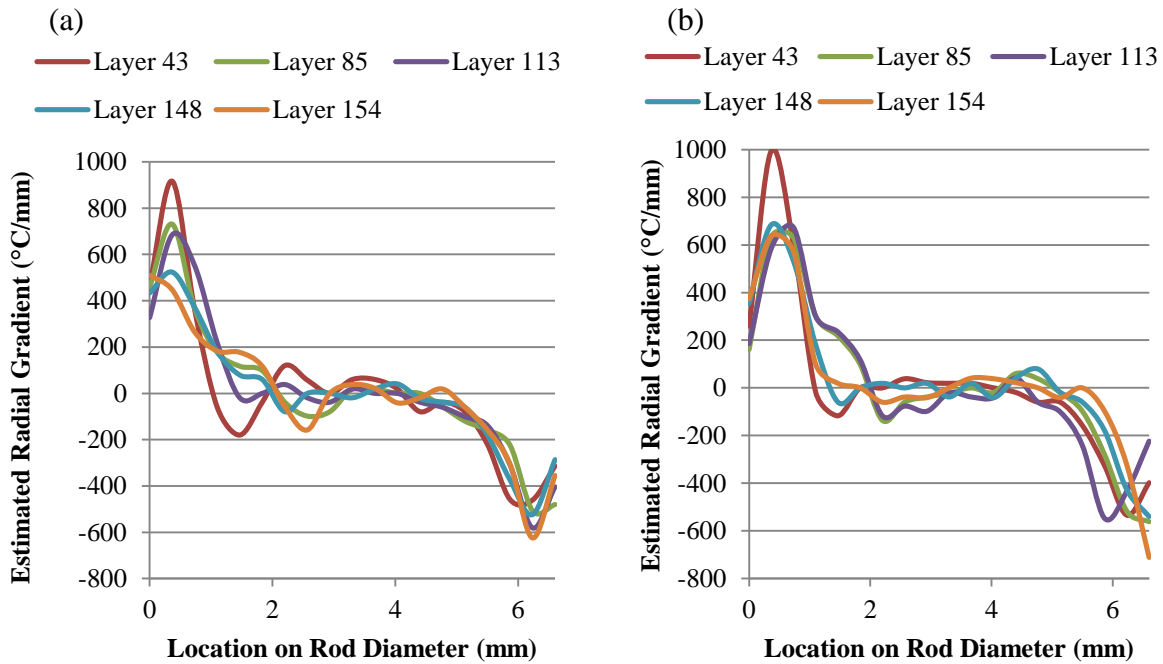


Figure 10. Plot of estimated radial gradients against location on rod diameter for (a) Pattern A and (b) Pattern B.

Conclusions

Using dual-thermography for non-destructive thermal inspection (NTI) of fabricated parts during Directed Energy Deposition (DED) processes such as Laser Engineered Net Shaping

(LENS) will be important for assessing part quality and microstructure in real-time. In a pyrometer/IR-camera setup, the melt pool temperature can be utilized for calibrating the IR camera which can be located in the LENS chamber. In this case, a near-constant calibration offset is feasible for a given temperature range. The current results indicate that the IR camera high-temperature can achieve accuracies on-the-order of 2-5 %.

Build-path temperature effects were not visibly discernable when varying the scan patterns for the cylindrical layers. However, upon analyzing thermographic data, temperature gradient magnitudes and cooling rates were found to vary along the radius of the melt pool and cylinder and this can influence final microstructure. For a given point in time and space, top-level layers were shown to have temperature characteristics more dependent on hatch pattern. Maximum melt pool temperature was observed to reach as high as 2500 °C and to be dependent on its contour track's starting point. The increase in melt pool temperature appeared to translate to an increase in cooling rate from about 16,000 °C/s - 41,000 °C/s for both investigated hatching patterns. Radial temperature gradients decreased with increasing layers; ranging between 500 °C/mm – 1000 °C/mm near the tail-end of the melt pool. The hatch pattern consisting of less layer revolutions appeared to have higher radial temperatures gradient, perhaps due to a mismatch of the patterns' deposition tracks.

Future work will aim to relate the observed thermal phenomena to determined microstructures using cooling rates based on the tail of the melt pool. A larger temperature range will be calibrated so that the IR camera may be more readily used for determining post solidification evolution. In addition, a black-body method of IR calibration will be investigated and employed to aid in determining emissivity of Ti-6Al-4V so that the results may be better compared to the values found in the literature. The results may also help in determining an “emissivity correction factor” for solidified regions of the part.

References

- [1] Griffith, M. L., Keicher, D. M., Atwood, C. L., Romero, J. a., Smugeresky, J. E., Harwell, L. D., Greene, D. L., 1996, “Free Form Fabrication of Metallic Components Using Laser Engineered Net Shaping (LENS),” *Proc. 7th Solid Free. Fabr. Symp.*, pp. 125–132, doi: 10.4028/www.scientific.net/AMR.15-17.175.
- [2] Smugeresky, J. E., Keicher, D. M., Romero, J. A., Griffith, M. ., Harwell, L. ., “Thermal behavior in the LENS process,” in *World Congress on Powder Metallurgy and Particulate Materials*, 1997.
- [3] Griffith, M. L., Schlienger, M. E., Harwell, L. D., Oliver, M. S., Baldwin, M. D., Ensz, M. T., Essien, M., Brooks, J., Robino, C. V, Smugeresky, J. E., Hofmeister, W. H., Wert, M. J., Nelson, D. V, 1999, “Understanding thermal behavior in the LENS process,” *Mater. Des.*, **20** (2)–(3), pp. 107–113, doi: 10.1016/S0261-3069(99)00016-3.
- [4] Griffith, M. L., Ensz, M. T., Puskar, J. D., Robino, C. V, Brooks, J. A., Philliber, J., Smugeresky, J. E., Hofmeister, W. H., “Understanding the microstructure and properties

- of components fabricated by laser engineered net shaping (LENS),” in *Materials Research Society Proceedings*, 2000.
- [5] Neela, V., De, a., 2009, “Three-dimensional heat transfer analysis of LENSTM process using finite element method,” *Int. J. Adv. Manuf. Technol.*, **45** (9)–(10), pp. 935–943, doi: 10.1007/s00170-009-2024-9.
- [6] Wang, L., Felicelli, S. D., Craig, J. E., 2007, “Thermal Modeling and Experimental Validation in the LENS Process,” *Proc. 2007 Solid Free. Fabr. Symp.*, pp. 100–111, doi: 10.1557/PROC-625-9.
- [7] Wang, L., Felicelli, S., 2006, “Analysis of thermal phenomena in LENS deposition,” *Mater. Sci. Eng. A*, **435–436** (1)–(2), pp. 625–631, doi: 10.1016/j.msea.2006.07.087.
- [8] Griffith, M. L., Schlienger, M. E., Harwell, L. D., Oliver, M. S., Baldwin, M. D., Ensz, M. T., Smugeresky, E., Essien, M., Brooks, J., Robino, C. V., Nelson, D. V., “Thermal behavior in the LENS process,” in *Proceedings of the 9th solid Freeform Fabrication Symposium, Austin, USA*, 1998, pp. 89–96.
- [9] Ye, R., Smugeresky, J. E., Zheng, B., Zhou, Y., Lavernia, E. J., 2006, “Numerical modeling of the thermal behavior during the LENS process,” *Mater. Sci. Eng. A*, **428** (1)–(2), pp. 47–53, doi: 10.1016/j.msea.2006.04.079.
- [10] Gaumann, M., Bezencon, C., Canalis, P., Kurz, W., 2001, “Single-Crystal Laser Deposition of Superalloys: Processing - Microstructure Maps,” *Acta Mater.*, **49**, pp. 1051–1062.
- [11] Hofmeister, W. ., Wert, M., Smugeresky, J. E., Philliber, J. A., Griffith, M. L., 1999, “Investigating solidification with the laser-engineered net shaping (LENS) process,” *JOM*, **51**, pp. 6–11.
- [12] Wang, L., Felicelli, S., Gooroochurn, Y., Wang, P. T., Horstemeyer, M. F., 2008, “Optimization of the LENS process for steady molten pool size,” *Mater. Sci. Eng. A*, **474** (1)–(2), pp. 148–156, doi: 10.1016/j.msea.2007.04.119.
- [13] Craig, J. E., Wakeman, T., Grylls, R., Bullen, J., 2011, “On-line imaging pyrometer for laser deposition processing,” *Sensors, Sampling, Simul. Process Control*, pp. 103–110.
- [14] Bi, G., Gasser, A., Wissenbach, K., Drenker, A., Poprawe, R., 2006, “Characterization of the process control for the direct laser metallic powder deposition,” *Surf. Coatings Technol.*, **201** (6), pp. 2676–2683, doi: 10.1016/j.surfcoat.2006.05.006.
- [15] Ocylok, S., Alexeev, E., Mann, S., Weisheit, A., Wissenbach, K., Kelbassa, I., 2014, “Correlations of Melt Pool Geometry and Process Parameters During Laser Metal Deposition by Coaxial Process Monitoring,” *Phys. Procedia*, **56**, pp. 228–238, doi: 10.1016/j.phpro.2014.08.167.

- [16] Nassar, A. R., Keist, J. S., Reutzel, E. W., Spurgeon, T. J., 2015, "Intra-layer closed-loop control of build plan during directed energy additive manufacturing of Ti-6Al-4V," *Addit. Manuf.*, **6**, pp. 39–52, doi: 10.1016/j.addma.2015.03.005.
- [17] Liu, S., Farahmand, P., Kovacevic, R., 2014, "Optical monitoring of high power direct diode laser cladding," *Opt. Laser Technol.*, **64**, pp. 363–376, doi: 10.1016/j.optlastec.2014.06.002.
- [18] Bi, G., Gasser, A., Wissenbach, K., Drenker, A., Poprawe, R., 2006, "Investigation on the direct laser metallic powder deposition process via temperature measurement," *Appl. Surf. Sci.*, **253** (3), pp. 1411–1416, doi: 10.1016/j.apsusc.2006.02.025.
- [19] Bi, G., Gasser, A., Wissenbach, K., Drenker, A., Poprawe, R., 2006, "Identification and qualification of temperature signal for monitoring and control in laser cladding," *Opt. Lasers Eng.*, **44** (12), pp. 1348–1359, doi: 10.1016/j.optlaseng.2006.01.009.
- [20] Yang, J., Sun, S., Brandt, M., Yan, W., 2010, "Experimental investigation and 3D finite element prediction of the heat affected zone during laser assisted machining of Ti6Al4V alloy," *J. Mater. Process. Technol.*, **210** (15), pp. 2215–2222, doi: 10.1016/j.jmatprotec.2010.08.007.
- [21] Doubenskaia, M., Pavlov, M., Grigoriev, S., Smurov, I., 2013, "Definition of brightness temperature and restoration of true temperature in laser cladding using infrared camera," *Surf. Coatings Technol.*, **220**, pp. 244–247, doi: 10.1016/j.surfcoat.2012.10.044.
- [22] Rodriguez, E., Mireles, J., Terrazas, C. a., Espalin, D., Perez, M. a., Wicker, R. B., 2015, "Approximation of absolute surface temperature measurements of powder bed fusion additive manufacturing technology using in situ infrared thermography," *Addit. Manuf.*, **5**, pp. 31–39, doi: 10.1016/j.addma.2014.12.001.
- [23] Purtonen, T., Kalliosaari, A., Salminen, A., 2014, "Monitoring and Adaptive Control of Laser Processes," *Phys. Procedia*, **56**, pp. 1218–1231, doi: 10.1016/j.phpro.2014.08.038.
- [24] Hagqvist, P., Sikström, F., Christiansson, A. K., 2013, "Emissivity estimation for high temperature radiation pyrometry on Ti-6Al-4V," *Meas. J. Int. Meas. Confed.*, **46** (2), pp. 871–880, doi: 10.1016/j.measurement.2012.10.019.
- [25] Kobryn, P. ., Semiatin, S. ., 2003, "Microstructure and texture evolution during solidification processing of Ti-6Al-4V," *J. Mater. Process. Technol.*, **135** (2)–(3), pp. 330–339, doi: 10.1016/S0924-0136(02)00865-8.
- [26] Ensz, M., Griffith, M., Harwell, L., "Software Development for Laser Engineered Net Shaping," in *Proceedings for the Solid Freeform Fabrication Symposium*, 1998, pp. 359–366.
- [27] Timet, "TIMET 6-4 Titanium Alloy (Ti-6Al-4V; ASTM Grade 5) Rod." .